Applied Physics Research; Vol. 5, No. 2; 2013
ISSN 1916-9639 E-ISSN 1916-9647
Published by Canadian Center of Science and Education

Investigation of Frequency Analysis Methods for Doppler Ultrasound Systems

Tatsuro Baba[1]

[1] Baba Professional Engineer Office, 1920-2, Usuba, Otawara, Tochigi, Japan

Correspondence: Tatsuro Baba, 1920-2, Usuba, Otawara, Tochigi 324-0035, Japan. Tel: 81-287-292-360. E-mail: EZD03014@nifty.ne.jp

Received: December 16, 2012 Accepted: January 18, 2013 Online Published: March 5, 2013
doi:10.5539/apr.v5n2p1 URL: http://dx.doi.org/10.5539/apr.v5n2p1

Abstract

Due to the advances of electronic and semiconductor technologies in recent years, it is possible to realize complex, low cost, low size, and low power consumption, high-speed signal processing devices. The progress of these devices has enabled the development of the medical Doppler ultrasound system. Color flow mapping (CFM), which is one of the display mode of Doppler ultrasound, requires high-speed multi-point (two- or three-dimensional) frequency analyses. From its birth till today, a complex autocorrelation (AC) method has been used for CFM because of its simplicity. In this paper, I propose the fast Fourier transform (FFT) method for the frequency analysis of CFM. CFM differs from spectrum Doppler, which shows accurate information of the blood flow in a narrow domain of a tomogram image. CFM uses color expression to display coarse information of the blood flow, such as mean velocity, intensity, and distribution. Because the calculation load of the frequency analysis is very small, the AC method has been used. However, by exploiting recent advances in hardware, new frequency analysis methods can be applied. In this paper, I evaluate a novel frequency analysis method based on FFTs, and compare its performance with the conventional AC method. Based on the results obtained, I reach the followings conclusions. With respect to mean velocity, the FFT method performs well when blood flow sensitivity is low. However, when blood flow sensitivity is high, the performance of the AC method is superior. Moreover, with respect to the distribution, compared to the FFT method, the AC method does not perform well under aliasing conditions. The AC method is effective only when the distribution is small.

Keywords: blood flow, complex autocorrelation, Doppler ultrasound, pulse pair, short-time Fourier transform

1. Introduction

Due to the advances of electronic and semiconductor technologies in recent years, it is possible to realize complex, low cost, low size, and low power consumption, high-speed signal processing devices. Thus, high performance signal processing can be realized more easily. In this paper, I investigated the frequency analysis of color flow mapping (CFM) of Doppler ultrasound systems, which has not changed since its introduction in the 1980s. In CFM processing, a high-order analog high-pass filter is used as a pre-processing step of the frequency analyzer. This filter is used to remove clatter (low-frequency and high-power noise) from the walls of blood vessels or heart. The dynamic range of the input of the frequency analyzer should be kept small. In the 1990s, new imaging techniques of mapping the clatter velocity became available, such as tissue Doppler imaging (TDI). In those days, it was difficult to simultaneously analyze blood flow and clatter. Because blood flow detection was not needed, TDI did not require a large dynamic range. However, in recent years, a high-dynamic range frequency analyzer can be easily realized using high-performance signal-processing devices. Since post filters following frequency analysis can be substituted, it is not necessary to use high-order pre filters. Blood velocity mapping in CFM is either two- or three-dimensional. Because the calculation load of the AC method is light, it is used since the introduction of CFM. Unlike the spectrum Doppler, which shows time frequency mapping, CFM represents roughly the blood flow parameters (mean velocity, distribution and power). Several types of short-time frequency analysis techniques are available. The short-time Fourier transform (STFT) method with a uniform time-frequency resolution is suitable for performing frequency analysis of nonstationary signals such as blood flow. In this paper, I propose a novel frequency analysis method for CFM. Specifically, I propose an FFT method and compare it with AC method.

2. CFM and Spectrum Doppler

Figure 1 shows spectrum Doppler and CFM images of fluid phantom. These images show the fluid flow in a silicon tube with a 3-mm diameter. The upper images are CFM images, while the lower images are spectrum Doppler images. The spectrum Doppler images indicate the power and velocity of the fluid flow in the tube. The horizontal axis represents time, while the vertical axis represents the velocity corresponding to the Doppler shift frequency. The spectrum Doppler images change with respect to the change of the blood flow velocity (0.2 to 1.0 m/s). Conversely, in CFM images, changes in the blood flow are represented by color variations. The features of CFM and spectrum Doppler are represented in Table 1. Because the clinical availability of CFM is existence of the blood flow, both its precision and resolution do not need high performance. Except for the calculation load, the FFT method (spectrum Doppler) is suitable for frequency analysis.

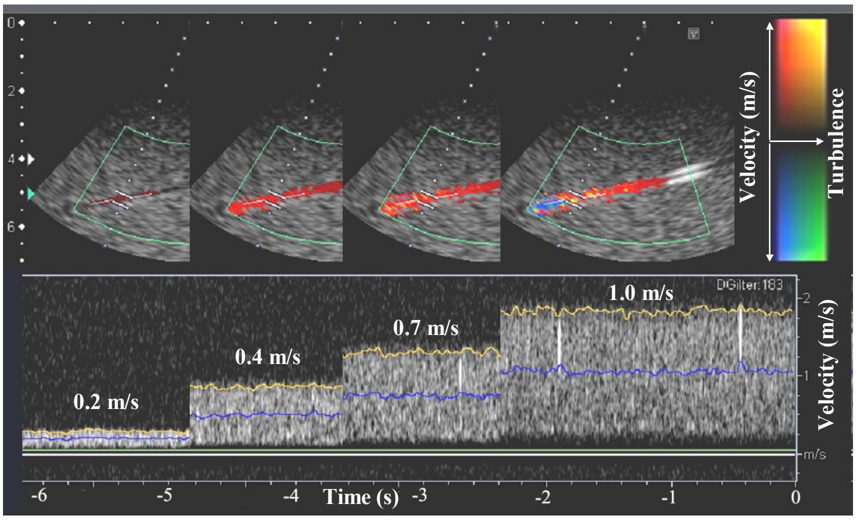

Figure 1. CFM and spectrum Doppler images

Table 1. Comparison of Doppler ultrasound diagnoses

Modality	CFM	Spectrum Doppler
Clinical availability	Existence of blood flow	Measurement of blood flow
Signal processing	AC method	FFT method
Output parameters	Total power, Mean velocity, Variance	Spectra, Mean velocity, Peak velocity
Precision/Resolution	Poor	Good
Calculation load	Small	Large

Due to hardware restrictions, early implementations of CFM adopted the AC method. Table 2 shows the calculation loads of the FFT (Figure 3) and AC methods (Figure 4). The calculation loads of both methods are estimated. Each pixel calculation requires N-time series. Because calculation load depends on the hardware architecture, I consider multiplication and addition as one-step operations, complex multiplication as a four-step operations and complex addition as a two-step operation. Moreover, we estimate memory access in signal processing by a 20% overhead of the total load.

Table 2. Estimations of calculation load of frequency analysis

(a) FFT method

Sub functions	Calculations	Steps
Window	(4) N	$4N$
FFT	(3) $N \times r$ + (4) $N \times r/2$	$4N \times r$
Power	(1) N + (2) $2N$	$3N$
Parameters	(1) $3N+1$ + (2) $3N+3$	$6N+4$
Overhead	(5) 20% of above total	-
Sum.	$(4N \times r + 13N + 4) \times 1.2$ [steps]	

(b) AC method

Sub functions	Calculations	Steps
$Q0$	(1) N + (4) N	$5N$
ω	(1) $2(N-1)$ + (4) $N-1$ + Table(*atan*( ))	$6N-5$
$Q2$	(1) $N-1$ + (2) $2(N-1)$ + Table(*sqrt*( ))	$3N-2$
Parameters	(1) 1 + (2) 1	2
Overhead	(5) 20% of above total	-
Sum.	$(14N-5) \times 1.2$ [steps]	

Notes 1: (1) Real add. (2) Real mul. (3) Comp. add. (4) Comp. mul. (5) Overhead.

Notes 2: $N=2^r$.

CFM images require 1.5×106 calculations/s (50000 pixels/frame and 30 frames/s). Table 3 shows calculation loads obtained by setting the time-series data N to 4, 8, and 16. Compared with the AC method, I see that the calculation load of the FFT method is approximately two times larger. Therefore, because the AC method has a light calculation load, it has been used until today.

Table 3. Calculation load of CFM

Data N	AC method	FFT method
4	9.3 *Mflops*	15.1 *Mflops*
8	19.4 *Mflops*	36.8 *Mflops*
16	39.5 *Mflops*	72.8 *Mflops*

3. Algorithm for Estimating Blood Flow Parameters

3.1 Definition of Blood Flow Parameters

In the CFM method, there are three types of blood flow parameters. The blood flow model in the frequency domain is shown in Figure 2. The average angular velocity, its distribution, and total spectrum power are defined as $\overline{\omega}$, σ^2 and *TP* respectively.

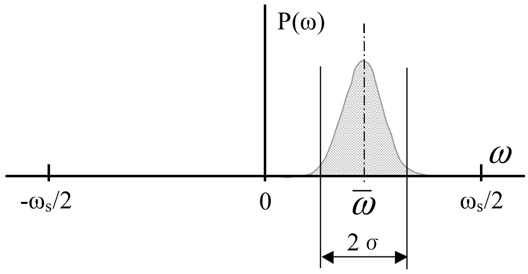

Figure 2. Definition of blood flow model

The parameters *TP*, $\overline{\omega}$, and σ^2 in Figure 2 are defined by Equations (1) to (3).

$$TP = \int_{-\omega_s/2}^{\omega_s/2} P(\omega) d\omega \tag{1}$$

$$\overline{\omega} = \frac{\int_{-\omega_s/2}^{\omega_s/2} \omega \cdot P(\omega) d\omega}{TP} \tag{2}$$

$$\sigma^2 = \frac{\int_{-\omega_s/2}^{\omega_s/2} (\omega - \overline{\omega})^2 \cdot P(\omega) d\omega}{TP} = \frac{\int_{-\omega_s/2}^{\omega_s/2} \omega^2 \cdot P(\omega) d\omega}{TP} - \overline{\omega}^2 \tag{3}$$

3.2 FFT Algorithm

The computational algorithm used by the FFT method is shown in Figure 3. In the calculation process, the power spectrum series P_i is used as temporary data. The middle data *P0*, *P1*, and *P2* (1st, 2nd and 3rd moments of spectra, respectively) are computed based on P_i. Next, these values are used to compute *TP*, $\overline{\omega}$, and σ^2.

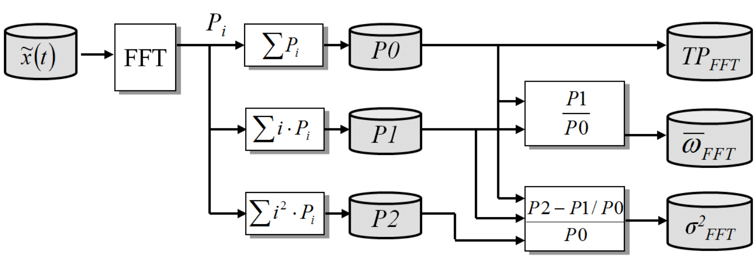

Figure 3. Algorithm of FFT method

The input signal $\tilde{x}(t)$ is a quadrature-detection output signal that is the Doppler-shift signals dropped into baseband. It is expressed in Equation (4) as the composition of multiple sinusoidal waveforms (amplitude a_i and phase ϕ_i).

$$\tilde{x}(t) = \sum^{i} a_i \cdot \exp(j \cdot \omega_i \cdot t) \cdot \exp(j \cdot \phi_i) \tag{4}$$

The FFT output $\tilde{Y}(j \cdot \omega_k)$ is denoted by Equation (5).

$$\begin{aligned}\tilde{Y}(j\cdot\omega_k) &= \sum^{i}\sum^{k} a_i \exp(j\omega_i t)\cdot\exp(j\varphi_i)\cdot\exp(-j\omega_k t) \\ &= \sum^{i}\sum^{k} a_i\cdot\exp\big(j(\omega_i-\omega_k)t\big)\cdot\exp(j\varphi_i)\end{aligned} \tag{5}$$

The power spectrum P_k of $\tilde{Y}(j\cdot\omega_k)$ is denoted by Equation (6).

$$P_k = \tilde{Y}(j\omega_k)\cdot\tilde{Y}^*(j\omega_k) = \sum^{i}\sum^{k} a^2{}_{i=k} = \sum^{i}\sum^{k} a_i{}^2 \tag{6}$$

When the FFT number is set to *N*, the moments are denoted by Equation (7).

$$P0 = \sum_{i=-N/2}^{N/2} P_i, \quad P1 = \sum_{i=-N/2}^{N/2} i\cdot P_i, \quad P2 = \sum_{i=-N/2}^{N/2} i^2\cdot P_i \tag{7}$$

Using Equations (1), (2), (3), and (7), we can compute the blood flow parameters, which are expressed by Equation (8). To compare with the AC method, the parameters are normalized by the FFT number *N*. Moreover, I normalized $\overline{\omega}$ by the sampling angle-frequency ω_s.

$$\begin{aligned}& TP_{FFT} = \frac{1}{N^2}\cdot P0, \quad \overline{\omega}_{FFT} = \frac{2\pi}{N}\cdot\frac{P1}{P0}, \\ & \sigma^2{}_{FFT} = \frac{P2 - P0\cdot P1^2}{N^2\cdot P0} = \frac{P2}{N^2\cdot P0} - \left(\frac{\overline{\omega}_{FFT}}{2\pi}\right)^2\end{aligned} \tag{8}$$

3.3 AC Algorithm

The computational algorithm used by the AC method is shown in Figure 4. The middle data *Q0*, *Q1*, and *Q2* (1^{st}, 2^{nd} and 3^{rd} moments corresponding to Equations (1) to (3), respectively) are calculated based on $\tilde{C}(0)$ and $\tilde{C}(\tau)$. These values are computed similar to the FFT method, while $\overline{\omega}$ and σ^2 are approximated.

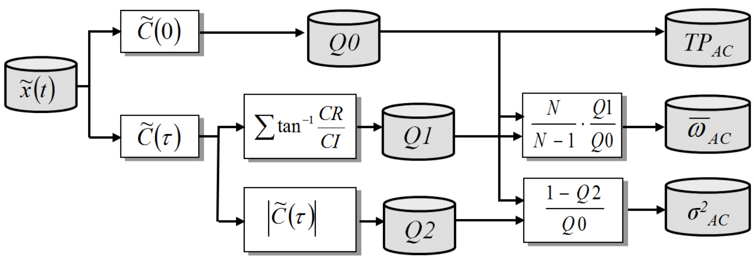

Figure 4. Algorithm of AC method

The frequency analysis of the AC method uses a complex autocorrelation (pulse pair) algorithm. Specifically, it multiplies the input signal $\tilde{x}(t)$ with the conjugate signal $\tilde{x}^*(t+\tau)$, which has a phase difference (sampling period τ).

$$\tilde{C}(\tau) = \sum^{N-1}\tilde{x}(t)\cdot\tilde{x}^*(t+\tau) = \sum_{i=1}^{N-1}\tilde{x}(i)\cdot\tilde{x}^*(i+1) = CR + j\cdot CI \tag{9}$$

Here, *CR* and *CI* are the real and imaginary parts of the (*N*－1) addition, and can be denoted by Equation (10).

$$CR = \sum_{j=1}^{N-1}\sum^{i} a_{ij}\cdot\cos(\omega_{ij}) \qquad CI = \sum_{j=1}^{N-1}\sum^{i} a_{ij}\cdot\sin(\omega_{ji}) \tag{10}$$

Equation (11) defines the moments *Q0*, *Q1*, and *Q2*. The expressions for *Q1* and *Q2* are approximations.

$$\begin{aligned} Q0 &= CR(0) = \sum_{j=1}^{N}\sum^{i} a_{ij}^{2}, \\ Q1 &= \sum_{j=1}^{N-1}\sum^{i} \omega_{ij}\cdot a_{ij}^{2} \cong \tan^{-1}\left(\frac{CI}{CR}\right)\cdot\sum_{j=1}^{N-1}\sum^{i} a_{ij}^{2}, \\ Q2 &= \sum_{j=1}^{N-1}\sum^{i} \omega_{ij}^{2}\cdot a_{ij}^{2} \cong \left(Q1^{2}+Q0^{2}-Q0\cdot\sqrt{CR^{2}+CI^{2}}\right)\cdot Q0 \end{aligned} \tag{11}$$

Using these moments, we compute TP, ϖ, σ^2 according to Equation (12). Here these parameters are normalized by time series N (for comparison with the FFT method), and ϖ is normalized by the range of $\pm\pi/2$.

$$\begin{aligned} TP_{AC} &= \frac{\tilde{C}(0)}{N}, \quad \varpi_{AC} = \frac{N}{N-1}\cdot\frac{Q1}{Q0}, \\ \sigma_{AC}^{2} &= \frac{\pi^{2}}{4}\cdot\left(\frac{\sqrt{CR^{2}+CI^{2}}}{Q0}-\left(\frac{Q1}{Q0}\right)^{2}\right) = \frac{\pi^{2}}{4}\cdot\left(1-\frac{Q2}{Q0}\right) \end{aligned} \tag{12}$$

4. Performances of Blood Flow Parameter Estimation

4.1 Single Sinusoidal Waveform Comparison

When the sinusoidal waveform $\tilde{x}(t) = a_i\cdot\exp(j\omega_i t)$ is applied to Equations (6) and (11), the TP_{FFT} and TP_{AC} values are obtained according to Equations (13) and (14), respectively. The values of TP_{FFT} and TP_{AC} are equal. Because a typical input signal consists of several sinusoidal waveforms (Equation (4)), TP_{FFT} and TP_{AC} are always equal.

$$TP_{FFT} = \frac{1}{N^2}\sum_{i=1}^{N}\ \sum_{k=1}^{N} a_{i=k}^{2} = a_i^{2} \tag{13}$$

$$TP_{AC} = \frac{1}{N^2}\cdot CR(0) = \frac{1}{N^2}\cdot\sum^{N}\ \sum_{i=1}^{N} a_i^{2} = a_i^{2} \tag{14}$$

The values of ϖ and σ^2 are plotted in Figures 5(a) and 5(b). The horizontal axis represents ϖ, which ranges from 0 to π/2. The time series N is set to 32. In Figure 5(a), although ϖ_{AC} is computed correctly, the discontinuity of the time window generates vibration on ϖ_{FFT}. These vibrations can be suppressed if a window function is applied prior to FFT processing. Moreover, because σ^2 is affected by the vibrations of ϖ, ${\sigma^2}_{FFT}$ becomes large. The results of parameter estimation are summarized in Table 4. Based on these results, I see that in general, the AC method is stable for a single sinusoidal waveform input.

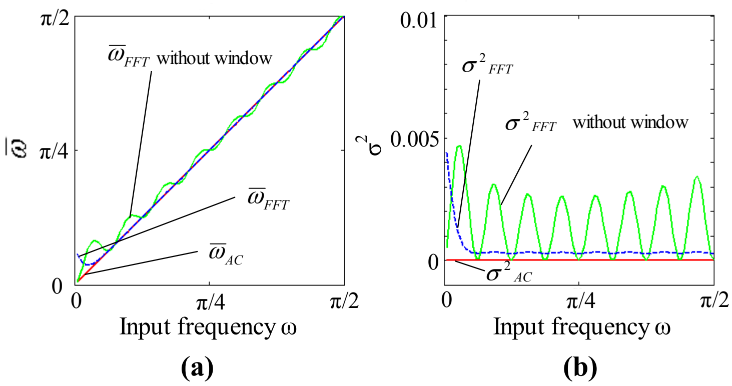

Figure 5. Simulation of a single sinusoidal waveform
Estimation of ϖ, (b) Estimation of σ^2

Table 4. Comparison of estimated parameters for a single sinusoidal waveform

Method	AC	FFT
TP	Correct	Correct
$\overline{\omega}$	Correct	Correct (preprocessing window is required)
σ^2	Correct	Affected by $\overline{\omega}$

4.2 σ^2 Comparison

First, we need to define the range of σ^2. For simplicity, I set $\overline{\omega}$ to 0 and compute the maximum value of σ^2. In Figure 6, I represent several types of σ^2 computational models. Figures 6 (a), (b), and (c) correspond to models of white noise and high-frequency noise and a pair of symmetrical sinusoidal waveforms, respectively. The corresponding distributions $\sigma^2{}_a$, $\sigma^2{}_b$, and $\sigma^2{}_c$ are obtained by Equation (15).

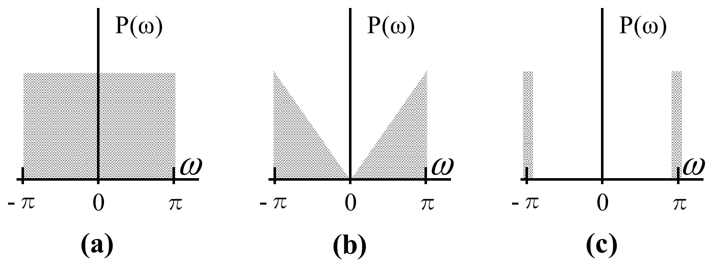

Figure 6. σ^2 range estimation models

(a) White noise, (b) High-frequency noise, (c) Pair of sine waves

$$
\begin{aligned}
\sigma_a{}^2 &= 2\int_0^{\pi} 1\cdot\omega^2 d\omega / 2\pi = \pi^2/3, \\
\sigma_b{}^2 &= 2\int_0^{\pi} \omega\cdot\left(\frac{\omega}{\tau}\right)^2 d\omega/\pi = \pi^2/2, \\
\sigma_c{}^2 &= \left(1\cdot\pi^2 + 1\cdot(-\pi)^2\right)/2 = \pi^2
\end{aligned}
\tag{15}
$$

This result indicates that the two-tone model (a pair of symmetrical sinusoidal waveforms shown in Figure 6(c)) achives the maximum range of σ^2. Figure 7 shows the estimated values of σ^2 obtained by this model. Figure 7(a) shows the input signal $\tilde{x}(t)$, which is a mixture of two-tone sine waves with $\omega_1 = \pi/40$ (near 0 Hz) and ω_2. The frequency difference $\omega_2 - \omega_1$ is expressed as $\Delta\omega$. As shown in Equation (16), the amplitudes of the two waveforms are equal.

$$\tilde{x}(t) = \exp(j\omega_1 t) + \exp(j\omega_2 t) \tag{16}$$

Figure 7(b) shows the estimated values of σ^2. Because aliasing occurs when $\Delta\omega$ exceeds $\pi/2$, $\overline{\omega}$ decreases and $\sigma_{AC}{}^2$ breaks at $\pi^2/4$. However, because all spectrum series are required in the calculation process of $\sigma_{FFT}{}^2$, the exact moments are computed based on baseline shift information. Because $\Delta\omega$ does not break until it reaches π, $\sigma_{FFT}{}^2$ can estimate the maximum value of π^2. The comparison of the estimated values of σ^2 is shown in Table 5. The comparison reveals that the range of $\sigma_{FFT}{}^2$ is larger than that of $\sigma_{AC}{}^2$, and $\sigma_{FFT}{}^2$ is stable.

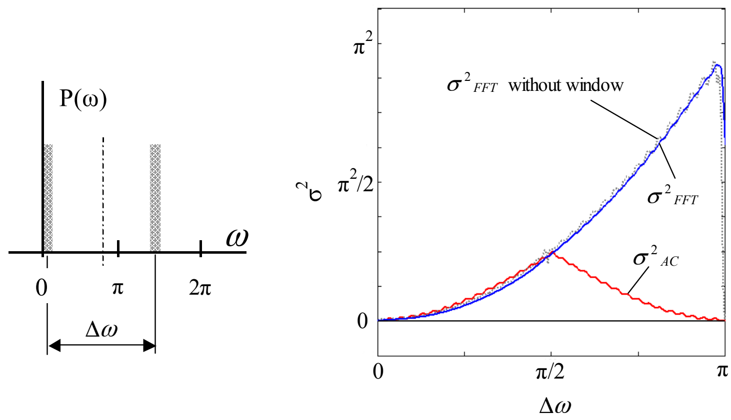

(a) (b)

Figure 7. Comparison of estimated values of σ^2 using two-tone sinusoidal waves
(a) Model of $\tilde{x}(t)$, (b) Estimation of σ^2

Table 5. Comparison of estimated values of σ^2 using two-tone sinusoidal waves

Method	AC	FFT
σ^2	Error at π/2～π caused by aliasing	Correct

4.3 Performance Comparison with Respect to Clatter

In Doppler ultrasound diagnosis, a high-intensity low-frequency signal (called clatter) is introduced into weak blood flow signals. Clatter is generated near walls of blood vessels or heart walls, and has a significant influence on the estimation of ϖ. I investigate the influence of clatter on ϖ using the two frequency signal inputs shown in Equation (17). Figure 8(a) shows the input signal model used, which has a clatter component (with angular frequency ω_1) and a blood flow component (with angular frequency ω_2). The power of clatter and blood flow is set to *P1* $(= a_1{}^2)$ and *P2* $(= a_2{}^2)$ respectively.

$$\tilde{x}(t) = a_1 \cdot \exp(j\omega_1 t) + a_2 \cdot \exp(j\omega_2 t) \tag{17}$$

The resulting estimated values of ϖ are shown in Figure 8 (b). Here, ω_1 and ω_2 are set to π /40 and π /5 respectively. I compute ϖ_{FFT} and ϖ_{AC} by changing the power ratios $P_1/P_2 (= a_1{}^2 / a_2{}^2)$ from –10 dB to +10 dB. ϖ_{FFT} is linearly related to *P1/P2* (has a dividing point) and is expressed by Equation (18).

$$\varpi_{FFT} = \frac{\omega_1 \cdot P_1 + \omega_2 \cdot P_2}{P_1 + P_2} = \frac{P_1}{P_1 + P_2} \cdot \omega_1 + \frac{P_2}{P_1 + P_2} \cdot \omega_2 \tag{18}$$

Conversely, ϖ_{AC} is equal to the angle between the synthetic vector of the component ω_1 ($P_1 \cdot \cos\omega_1 + jP_1 \cdot \sin\omega_1$) and that of ω_2 ($P_2 \cdot \cos\omega_2 + jP_2 \cdot \sin\omega_2$), and is expressed by Equation (19). Therefore, ϖ_{AC} and *P1/P2* are non-linearly related, and ϖ_{AC} decreases as *P1/P2* increases. The comparison results of ϖ are presented in Table 6. The estimated values of ϖ_{AC} are lower in the presence of clatter.

$$\varpi_{AC} = \tan^{-1}\left(\frac{P_1 \cdot \sin\omega_1 + P_2 \cdot \sin\omega_2}{P_1 \cdot \cos\omega_1 + P_2 \cdot \cos\omega_2}\right) \tag{19}$$

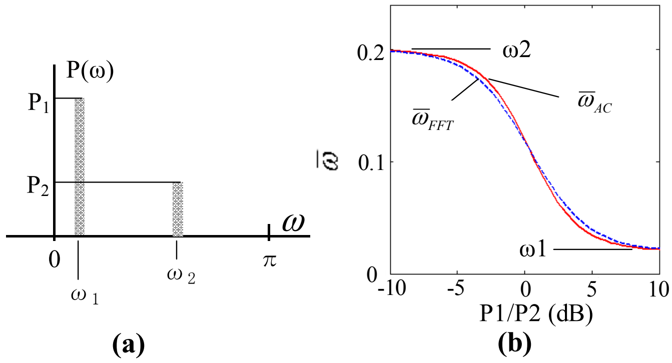

Figure 8. Comparison of estimated values of $\overline{\omega}$ using two-tone sinusoidal waves

(a) Model of $\tilde{x}(t)$, (b) Estimation of $\overline{\omega}$

Table 6. Comparison of $\overline{\omega}$ affected due to clatter

Method	AC	FFT
$\overline{\omega}$	Affected by clatter: Under estimation at P1/P2 > 0dB	Correct

4.4 Performance Comparison with Respect to Noise (Influence on $\overline{\omega}$)

In Doppler ultrasound diagnosis, the sensitivity of blood flow plays an important role in CFM. Even when S/N is poor, exact blood flow estimation is required. To investigate the influence of noise on $\overline{\omega}$, I use the model of $\tilde{x}(t)$ shown in Figure 9(a), which is a mixture of white noise and a single sinusoidal waveform. The noise to signal ratio is denoted by α (the power ratio of the ω_0 component), and noise is uniformly distributed from $-\pi$ to π. The 0th and 1st moments, N_0 and N_1, respectively, of noise are expressed by Equation (20). Because the 1st moment is an odd function, N_1 becomes zero.

$$
\begin{aligned}
N_0 &= \int_{-\pi}^{\pi} P_{noise}(\omega) d\omega = 2\pi\alpha, \\
N_1 &= \int_{-\pi}^{\pi} \omega \cdot P_{noise}(\omega) d\omega = \alpha \int_{-\pi}^{\pi} \omega d\omega = 0
\end{aligned}
\tag{20}
$$

When the 0th and 1st moments of ω_0 are set to $P0_{\omega 0}$ and $P1_{\omega 0}$ respectively, I can use the expression of N_1 and N_2 of Equation (20) and obtain the expression of $\overline{\omega}_{FFT}$ shown in Equation (21).

$$
\overline{\omega}_{FFT} = \frac{N_1 + P1_{\omega_0}}{N_0 + P0_{\omega_0}} = \frac{\omega_0}{2\pi\alpha + 1} \tag{21}
$$

In the AC method, I compute $\overline{\omega}_{AC}$ using the angle of $\tilde{C}(\tau)$ in complex coordinates expressed by Equation (9). The white noise component $\alpha(\delta_r, j\delta_i)$ is added to the tip of the ω_0 component. As shown in Figure 9(b), the velocity vector is distributed on a concentric circle with radius α. Here, $(\delta_r, j\delta_i)$ represents the complex random noise.

$$
\overline{\omega}_{AC} = \tan^{-1}\left(\frac{\sum_{i=1}^{N-1} \left(1 \cdot \sin(i \cdot \omega_0 / 2\pi) + \alpha \cdot \delta_i\right)}{\sum_{i=1}^{N-1} \left(1 \cdot \cos(i \cdot \omega_0 / 2\pi) + \alpha \cdot \delta_r\right)} \right) \tag{22}
$$

When the average autocorrelation (with number *N–1*) is calculated using Equation (22), the synthetic vector converges on the center of a concentric circle and can be approximated using Equation (23).

$$\lim_{N\to\infty} \overline{\omega}_{AC} = \omega_0 \tag{23}$$

The simulation results obtained using Equation (24) show that the noise ratio α changes from –10 dB to 10 dB. The results are presented in Figure 9(c).

$$\tilde{x}(t) = \exp(j\omega_0 t) + \alpha(\delta_r, j\delta_i) \tag{24}$$

Here, ω_0 is set to π/5.

When the noise level is lower than the signal level, $\overline{\omega}_{FFT}$ decreases and $\overline{\omega}_{AC}$ is not easily affected by noise. Moreover, when the signal level is lower than the noise level, $\overline{\omega}_{AC}$ also decreases and its accuracy is less than that of $\overline{\omega}_{FFT}$ (α exceeds 8 dB in Figure 9(c)).

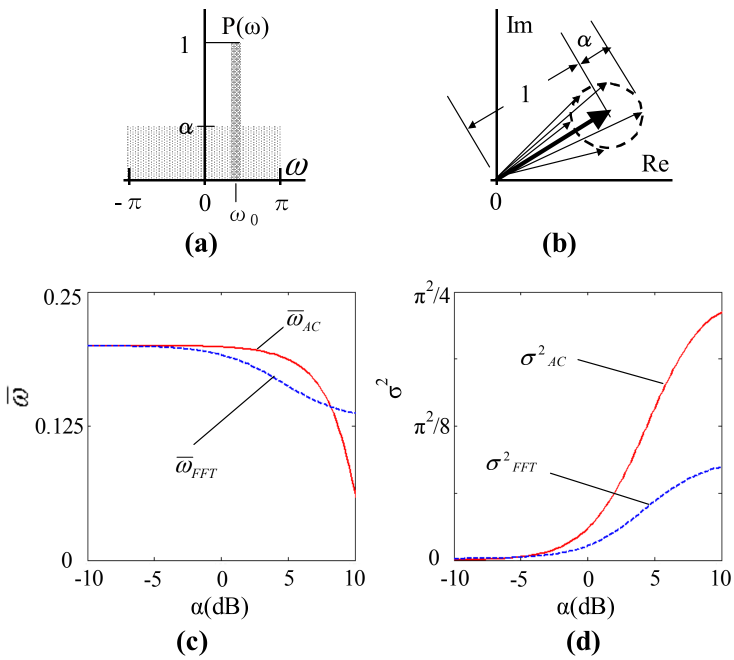

Figure 9. Simulations of white-noise model

(a) Model of $\tilde{x}(t)$, (b) AC Model of $\tilde{x}(t)$, (c) Estimation of $\overline{\omega}$, (d) Estimation of σ^2.

4.5 Performance Comparison with Respect to Noise (Influence on σ^2)

Next, I set ω_0 to zero in Equation (24) and compare the performance of σ^2. The norm of the synthetic vector in the AC method, *NORM*, is obtained by Equation (25).

$$\begin{aligned} NORM &= \sqrt{\left(\sum_{i=1}^{N-1}\left(\frac{1}{\sqrt{N}} + \alpha\cdot\cos\left(\frac{i}{N}\cdot 2\pi\right)\right)\right)^2 + \left(\sum_{i=1}^{N-1}\left(\frac{1}{N} + \alpha\cdot\sin\left(\frac{i}{N}\cdot 2\pi\right)\right)\right)^2} \\ &\cong \sqrt{N\left(\frac{1}{N} + \frac{\alpha}{2}\right)^2} \end{aligned} \tag{25}$$

Here, in the domain $0 \le 2\pi\cdot i/N \le \pi$, I generate vectors with equal imaginary parts ($0 \le 2\pi\cdot i/N \le \pi/2$ and $\pi/2 \le 2\pi\cdot i/N \le \pi$). Because $TP_{AC} = 1 + \alpha^2\cdot N$, the average of these synthetic vectors is regarded as $(1, \alpha/\sqrt{N})$. The value of σ_{AC}^2 is obtained by Equation (26).

$$\sigma_{AC}^{\ 2} = \frac{\pi^2}{4}\left(1 - \frac{NORM}{TP_{AC}}\right) = \frac{\pi^2}{4}\left(1 - \frac{\sqrt{1 + \frac{N}{2}\cdot\alpha^2}}{1 + \alpha^2\cdot N}\right) \tag{26}$$

In the FFT method, TP_{FFT} and $P2$ are obtained as follows;

$$TP_{FFT} = 1 + \alpha^2 \cdot N\,,\quad P2 = 2 \cdot \sum_{i=1}^{N/2} \left(\frac{i}{N} \cdot \pi - \varpi_{FFT} \right)^2 \cdot \alpha^2 \quad ,$$

The value of $\sigma_{FFT}{}^2$ is denoted by Equation (27).

$$\begin{aligned} \sigma_{FFT}{}^2 &= \frac{2\pi^2 \cdot \alpha^2}{\left(1+\alpha^2 N\right) \cdot N^2} \cdot \frac{N\left(N+1\right)\left(N+2\right)}{24} \\ &= \frac{\pi^2 \cdot \alpha^2}{12} - \frac{\left(N+1\right)\left(N+2\right)}{\left(1+\alpha^2 N\right) \cdot N} \end{aligned} \tag{27}$$

Because it is difficult to directly compare Equations (26) and (27), in Figure 9(d), I present the simulation results for $\sigma_{FFT}{}^2$ and $\sigma_{AC}{}^2$ obtained by changing the value of α in Equation (24) from –10 to 10 dB. The AC method tends to be affected by noise. When the noise level increases, the accuracy of ϖ_{AC} deteriorates and the value of $\sigma_{AC}{}^2$ increases. The performance characteristics of the two methods with respect to noise are summarized in Table 7.

Table 7. Comparison of ϖ and σ^2 affected due to noise

Method	AC	FFT
ϖ	Not affected by noise at low noise condition	Under estimated at low noise condition
σ^2	Affected by noise at high noise condition	Correct

5. Considerations

In Section 4, I investigated the fundamental characteristics of the blood flow parameters (*TP,* ϖ and σ^2) using a simple sinusoidal input signal. However, because in actual blood flow the velocity changes, in this section, I investigate the characteristics of blood flow parameters using a wide-band waveform. For example, in the current CFM processing, when ϖ becomes large, σ^2 increases. This occurs because Equation (12) is an approximate expression. Therefore, the display of turbulent flow in conventional CFM systems cannot distinguish whether it depends on wide-band blood flow or on measurement errors. This is a problem when using CFM as a blood flow measurement system. In Figure 10, I compare the estimated values of ϖ and σ^2 obtained by the the AC and FFT methods. In Figure 10(a), I present the frequency fluctuation model where its input signal $\tilde{x}(t)$ (Equation (28)) is frequency modulated by the noise signal $\tilde{N}(t)$ (with central angular frequency ω_1 and band-width β). In Figure 10, ω_1 is set to $\pi/10$ and β is changed from 0.02π to 2π.

$$\tilde{x}(t) = \exp(j\omega_1 t + j \cdot \beta \cdot \tilde{N}(t)) \tag{28}$$

In the AC method, $\sigma_{AC}{}^2$ corresponds to the variation of the synthetic vector shown in Figure 10(b). The real part *Re* and, imaginary part *Im*, synthetic vector angle θ, norm of synthetic vector *NORM*, and total power TP_{AC} are expressed by Equations (29), (30), (31), and (32), respectively.

$$\mathrm{Re} = \sum_{i=1}^{N-1} \cos\left(\frac{i}{N} \cdot \beta \cdot \pi \right) \qquad \mathrm{Im} = \sum_{i=1}^{N-1} \sin\left(\frac{i}{N} \cdot \beta \cdot \pi \right) \tag{29}$$

$$\theta = \frac{1}{2} \tan^{-1}\left(\frac{\mathrm{Im}}{\mathrm{Re}} \right) \tag{30}$$

$$NORM = \sqrt{\left(\sum_{i=1}^{N-1} \cos\left(\frac{i}{N} \cdot \beta \cdot \pi \right) \right)^2 + \left(\sum_{i=1}^{N-1} \sin\left(\frac{i}{N} \cdot \beta \cdot \pi \right) \right)^2} \tag{31}$$

$$TP_{AC} = \sum_{i=1}^{N}\left(\cos^2\left(\frac{i}{N}\cdot\alpha\cdot\pi\right)+\sin^2\left(\frac{i}{N}\cdot\alpha\cdot\pi\right)\right) = N \tag{32}$$

Using Equations (29), (30), (31), and (32), I obtain Equation (33), which expresses $\sigma_{AC}{}^2$

$$\begin{aligned}\sigma_{AC}{}^2 &= \frac{\pi^2}{4}\left(1-\frac{NORM}{TP_{AC}}\right)\\ &= \frac{\pi^2}{4}\left(1-\frac{\sqrt{\left(\sum_{i=1}^{N-1}\cos\left(\frac{i}{N}\beta N\right)\right)^2+\left(\sum_{i=1}^{N-1}\sin\left(\frac{i}{N}\beta N\right)\right)^2}}{N}\right)\end{aligned} \tag{33}$$

In the FFT method, TP_{FFT} and $P2$ are denoted by Equations (34) and (35), respectively.

$$TP_{FFT} = \sum_{i=1}^{N-1}\left(\cos^2\left(\frac{i}{N}\cdot\beta\cdot\pi\right)+\sin^2\left(\frac{i}{N}\cdot\beta\cdot\pi\right)\right) = N \tag{34}$$

$$P2 = 2\cdot\sum_{i=1}^{N/2}\left(\frac{i}{N}\cdot\alpha\cdot\pi-\varpi_{FFT}\right)^2\cdot 1 \tag{35}$$

Using Equations (8), (34), and (35), Equation (36) is obtained, which expresses $\sigma_{FFT}{}^2$.

$$\begin{aligned}\sigma_{FFT}{}^2 &= \frac{2}{N}-\frac{2\pi^2\cdot\beta^2}{N^2}\cdot\sum_{i=1}^{N/2} i^2\\ &= \frac{\pi^2\beta^2}{12}\cdot\frac{(N+1)(N+2)}{N^2}\end{aligned} \tag{36}$$

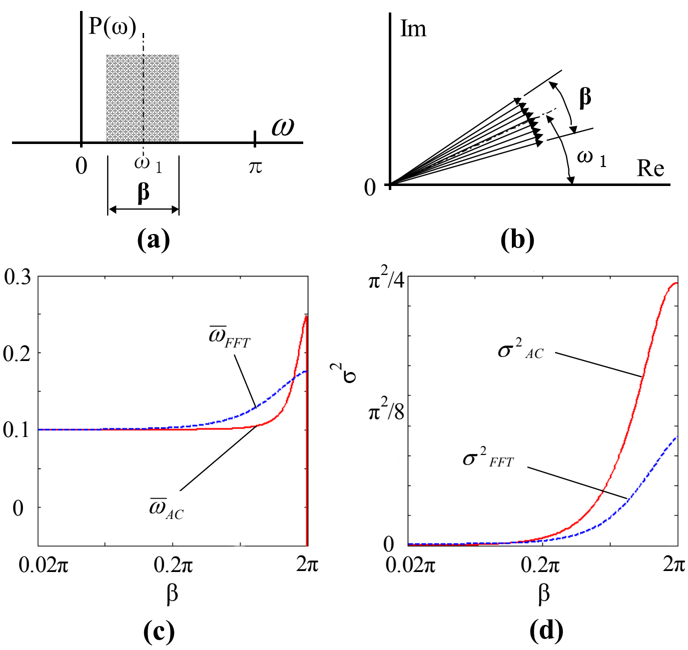

Figure 10. Simulations of wide-band model

(a) Model of $\tilde{x}(t)$, (b) AC Model of $\tilde{x}(t)$, (c) Estimation of ϖ, (d) Estimation of σ^2

Because it is difficult to directly compare Equations (33) and (36), I present the estimation results of $\sigma_{FFT}{}^2$ and

$\sigma_{AC}{}^2$ obtained by changing the parameter β of the input signal in Figure 10(d). In general, the influence of the distribution generated by frequency modulation in the AC method is larger than that in the FFT method. In Figure 10(c), I see that when the fluctuation width is small (β is smaller than π), ϖ_{AC} becomes more stable than ϖ_{FFT}. Conversely, when the fluctuation width is large, ϖ_{AC} becomes unstable. In Table 8, I summarize my findings on how the bandwidth (wide-band model) influences the values of ϖ and σ^2.

Table 8. Comparison of ϖ and σ^2 affected by a wide-band signal

Method	AC	FFT
ϖ	Affected by wide-band at high bandwidth $\beta > \pi$	Over estimated at low bandwidth
σ^2	Over estimated	Correct

6. Conclusions

Since the introduction of CFM, frequency analysis based on the AC method has been used. Because the AC method has light calculation load and is easily implemented, it was thought to be the best solution for CFM processing. For example, its calculation load is half of that of the FFT method. Due to the recent advances in signal-processing devices, hardware size is no longer an issue, which enables the use of the FFT method in CFM processing. Hence, we used mathematical expressions and simulations and performed a comparative evaluation of the performance of the conventional AC method and the new FFT method. The results show that when blood flow sensitivity is low, the performance of the FFT method for computing mean velocity in the presence of clatter or noise is good. Conversely, when blood flow sensitivity is high, the AC method achieves excellent performance. Moreover, compared with the FFT method, the distribution in the AC method is weak under aliasing conditions. It turns out that the AC method is effective only when the distribution is small.

References

Baba, T. (2007). Direction separation in Doppler audio ultrasound diagnosis equipment: Signal processing for Doppler audio dealiasing. *Acoust. Sci. & Tech., 28*(3), 202-210. http://dx.doi.org/10.1250/ast.28.202.

Baba, T. (2009). *Acoustical Imaging 29: Evaluation of post wall filter for Doppler ultrasound systems* (pp.133-138). Springer Science+Business Media B.V. http://dx.doi.org/10.1007/978-1-4020-8823-0_19

Baba, T. (2010). Ultrasound Diagnostic Apparatus. *Japanese Patent No.* 4,481,386. Toshiba Corp.

Baba, T. (2011). *Applications of Digital Signal Processing: Complex Digital Filter Designs for Audio Processing in Doppler Ultrasound System*. Rijeka Croatia: INTECH. http://dx.doi.org/10.5772/25958

Baba, T. (2012). Time-frequency analysis using short time Fourier transform. *The Open Acousitics Journal, 5*, 32-38. http://dx.doi.org/10.2174/1874837601205010032

Baba, T. (2013). *Design and Architectures for Digital Signal Processing: Progress of Doppler ultrasound system design and architectures*. Rijeka Croatia: INTECH. http://dx.doi.org/10.5772/51508

Bjaerum, S., Torp, H., & Kristoffersen, K. (2002). Clutter filter design for ultrasound color flow imaging. *IEEE Trans. on UFFC, 49*(2), pp.204-216. http://dx.doi.org/10.1109/58.985705

Cohen, L. (1995). *Time Frequency Analysis: Theory and Applications*. New Jersey: Prentice-Hall PTR.

Ishida T. et al. (2010). *HANDBOOK of Medical Imaging*. Tokyo: Ohmsha.

Jensen, J. A. (1996). *Estimation of Blood Velocities Using Ultrasound: A Signal Processing Approach*. New York: Cambridge University Press.

Kanai, H., & Koiwa, T. (2001). Myocardial rapid velocity distribution. *Ultrasound in Medicine and Biology, 27*(4), 481-498. http://dx.doi.org/10.1016/S0301-5629(01)00341-6

Rabben, S. I., Bjaerum, S. et al. (2002). Ultrasound-based vessel wall tracking: an auto-correlation technique with RF center frequency estimation. *Ultrasound in Medicine and Biology, 28*(4), 507-517. Retrieved from http://www.umbjournal.org/article/S0301-5629(02)00487-8/abstract

Sato, S., Yoshikawa, A., & Kiryu, T. (2004). *Introduction to Biosignal Processing*. Tokyo: Corona publishing co. Ltd.

Semmlow, J. L. (2009). *Biosignal and Medical Image Processing* (2nd ed.). Boca Raton, FL: CRC Press.